Earth and Planetary Science Letters 524 (2019) 115713

Contents lists available at ScienceDirect

Earth and Planetary Science Letters

www.elsevier.com/locate/epsl

In situ evidence of earthquakes near the crust mantle boundary initiated by mantle CO_2 fluxing and reaction-driven strain softening

Bjørn Eske Sørensen *, Thomas Grant, Eric James Ryan, Rune B. Larsen

Department of Geoscience and Petroleum, Norwegian University of Technology and Science (NTNU), Sem Sælands vei1, 7491 Trondheim, Norway

ARTICLE INFO

Article history:
Received 7 March 2019
Received in revised form 27 June 2019
Accepted 12 July 2019
Available online 2 August 2019
Editor: J. Brodholt

Keywords:
CO_2
CO_2 emission
grain size sensitive creep
reaction driven strain softening
earthquake
olivine

ABSTRACT

This study aims to understand the process behind the worldwide connection between deep crustal/upper mantle earthquakes and CO_2 emissions along faults in rift zones. We do this by studying CO_2-induced mineral reactions that facilitate strain localization in peridotites from an ancient rift zone in the Seiland Igneous Province (SIP), North Norway.

Strain localization in association with hydration processes is well documented in all types of tectonic settings and has major implications for rheological behavior in active plate margin processes. The implications of CO_2-bearing fluids are less studied, though experiments have shown how CO_2 can influence the flow laws of olivine by imposing a brittle and more localized type of deformation.

This study documents narrow shear zones observed within ultramafic rocks from the Seiland Igneous Province (SIP) comprising large volumes (>20,000 km^3) of mafic, ultramafic, silicic and alkaline melts that were emplaced into the lower continental crust (25–30 km) between 570 and 560 Ma under an extensional regime. The extensional shear zones are mm cm-scale and contain extremely fine-grained material with a distinct shape preferred orientation (SPO), but weak to absent crystallographic preferred orientation. The shear zones offset dykes across numerous micro-faults that are documented in areas close to a major fault zone cutting through the area. Within the shear zones, olivine and clinopyroxene react to form orthopyroxene and dolomite at approximately 11 kb and 850 °C according to the reaction:

2 Olivine + Clinopyroxene + 2 CO_2 = Dolomite + 2 Orthopyroxene

This reaction formed coronas of orthopyroxene and dolomite between olivine and clinopyroxene in the shear zones. In addition, large olivine grains proximal to the shear zones show a microfabric with subgrain walls decorated by rounded grains of dolomite and more irregular and elongated grains of orthopyroxene. Clinopyroxene grains are separated from the enstatite and dolomite by at least hundreds of microns, suggesting material transport within the shear zone. The shear zones thus provide a unique insight into the interplay between CO_2-metasomatism and reaction accommodated strain softening. Carbonation-driven cracking and mineral reaction also serves to reduce grain size, making grain boundary sliding an efficient process, further enhancing the rheological contrast between the shear zone and the host rock. The sudden decrease in rock strength could lead to rapid deformation and triggered pseudotachylite formation during earthquake events in the near proximity of the micro-shear zones. Our observations match the relations between CO_2 emissions and earthquakes observed in present rift environments such as the East African rift and in New Zealand, and underline the importance of active shear zones as fluid conduits in the lower crust and upper mantle.

1. Introduction

The flux of CO_2 from the mantle, through the crust, and into the atmosphere in large igneous provinces and continental rifts may alter the global climate and is linked to mass extinction events (Brune et al., 2017; Foley and Fischer, 2017; Wignall, 2001). Although large amounts of CO_2 can be released from magmas through degassing, in areas with no, or low amounts of volcanic activity, seeping along deep crustal faults is considered to be a primary source of atmospheric CO_2 (Lee et al., 2016). Lower crustal seismicity and earthquake swarms around the margins of velocity anomalies interpreted as intrusions are also well documented in these areas, such as in the East-African rift (Lee et al., 2016; Roecker et al., 2017; Weinstein et al., 2017) and New Zealand (Reyners et al., 2007). The depths at which these earthquakes occur (30–40 km), is close to the depths at which CO_2 is released

* Corresponding author.
E-mail address: bjorn.sorensen@ntnu.no (B.E. Sørensen).

https://doi.org/10.1016/j.epsl.2019.115713

from basaltic melts (Dixon, 1997; Gerlach et al., 2002), implying a link between lower crustal seismicity and CO_2 fluids (Lindenfeld et al., 2012; Okubo and Wolfe, 2008; Takeuchi and Arai, 2015; Wilshire and Kirby, 1989). This is supported by fluid dynamic models (Balmforth et al., 2005). There is also evidence of the fluxing of mantle-derived CO_2 along major shear zones rooted in the mantle (Pili et al., 1997, 1999). However, the mechanisms by which CO_2 fluids initiate seismic events in the deep crust or upper mantle remains poorly understood, and is mostly based on theoretical modeling and observations correlating mantle derived CO_2 emissions along fault zones in the east-African rift and lower crustal seismicity (Hunt et al., 2017; Lee et al., 2016; Roecker et al., 2017; Weinstein et al., 2017).

The role of H_2O during deformation of ultramafic rocks in the lower crust and upper mantle is relatively well studied, yet little is known about the effects of CO_2. Experiments and observations on xenoliths in basalt have shown that CO_2 can influence the flow laws of olivine by imposing a brittle, and more localized type of deformation (Rovetta et al., 1987, 1986). Fluids rich in CO_2 are abundant and highly reactive in the upper mantle. Reactions between these CO_2 fluids and ultramafic rocks leads to carbonates (Wyllie et al., 1983). However, evidence of these reactions in mantle xenoliths may be destroyed during decompression and/or later heating (Canil, 1990; Canil and Scarfe, 1990). There is potential for both deformation and metasomatism in the upper mantle and lower crustal rocks in the presence of CO_2-rich fluids.

Here, we present data from a deep crustal ultramafic intrusion associated with Ediacaran continental rifting and the break-up of Rodinia (Larsen et al., 2018), which record the mechanisms by which CO_2 fluids induce deformation in peridotite. This work provides a missing link in understanding the processes through which CO_2 may catalyze deep crustal faulting during fluxing from the upper mantle, through the lower crust, and into the atmosphere along deep crustal fault zones.

2. Geological setting and sampling localities

The Seiland Igneous Province (SIP) in Northern Norway, contains an exposure of more than 5000 km^2 of mafic and ultramafic intrusions with minor alkaline, carbonatite and felsic rocks, intruded into the lower continental crust at depths of 25 to 35 km. The SIP is geochemically and temporally correlated to dyke swarms throughout Scandinavia at 560–610 Ma and is linked to magmatic provinces in W-Greenland and NE-America collectively known as the Central Iapetus Magmatic Province (CIMP) (Larsen et al., 2018).

Revised mapping shows that the SIP exposures are 85–90% layered tholeiitic-alkaline- and syeno-gabbros, 8–10% peridotitic complexes, 2–4% carbonatite, syenite and diorite. All of the intrusive bodies formed within a narrow ($<$10 Ma) time frame in the Ediacaran (560–570 Ma) (Roberts et al., 2006). The ultramafic complexes in the SIP comprise deep-seated transient magma chambers that facilitated mixing and homogenization of a rich diversity of fertile asthenospheric melts en-route to the upper parts of the continental crust (Larsen et al., 2018).

For this study we mapped and sampled one of these conduits, the Reinfjord Ultramafic Complex, in the southwestern part of the SIP, which consists of modally and cryptically layered dunites, wehrlites and olivine clinopyroxenites formed through multiple recharge events (Grant et al., 2016) (Fig. 1a). The widespread occurrence of clusters of dolomite bearing metasomatic assemblages Grant et al. (2016) suggest that the cumulates were infiltrated by a late CO_2-rich melt phase that was most likely co-genetic with the melts that formed the rest of the intrusion (Larsen et al., 2018). The ultramafic rocks are transected by a km scale fault, which can be recognized as an escarpment in the landscape, filled with snow (Fig. 1a). Asymmetric folding in the footwall (western block of the fault) documents that the fault is extensional with down throw of the eastern block on an eastward dipping fault plane (Fig. 1b). The central part of the fault is rarely exposed and is intensely altered by later serpentinization. However, a well-preserved sample was recovered, displaying ultramafic pseudotachylites (Fig. 1a and d). The pseudotachylites are recognized in the field as mm-thick dark planes, with a spacing of 0.5–1 cm (Fig. 1d). Micro shear zones with carbonation reactions are common throughout the area, but later serpentinization commonly overprints the carbonation related textures. In areas with pyroxenite dykes the micro shear zones intersect and offset pyroxenite dykes (Fig. 1c). A well-preserved micro shear zone sample was selected for more detailed studies (Fig. 1e).

3. Methods

3.1. EPMA (Electron Probe Micro Analysis)

Mineral data was obtained at NTNU, Trondheim using a JEOL JXA-8500F thermal field emission electron probe micro-analyzer (EPMA). Silicates and oxides were analyzed with 15 KeV and 20 nA using mineral and metal standards. Beam widths were fully focused to 1 µm for olivine, orthopyroxene, clinopyroxene and oxides. Wider beams of 2 µm were used for amphibole. Special care was taken when analyzing dolomite by using lower beam currents of 5 nA and the widest beams possible for the size of the grains ($>$5 µm), closely following the method described in Franzolin et al. (2011).

3.2. EBSD (Electron Backscatter Diffraction)

Standard oriented thin sections, cut orthogonal to the foliation and parallel to the stretching lineation, were used for petrographic investigations and to investigate the crystallographic preferred orientation (CPO) of the vein-related quartz by EBSD analysis at the Scanning Electron Microscope (SEM).

To remove surface damage and thereby enhance the diffraction signal, the thin sections were polished using colloidal silica for 5 min (Moen et al., 2003) and placed in a Hitachi VP-SEM with a Nordif UF-1000 EBSD detector (Chen et al., 2012) at a 70 tilt to the horizontal (Prior et al., 2009).

To acquire satisfactory pattern quality, the accelerating voltage used was 20.0 kV at 34 nA absorbed current. This was done as a compromise between high signal and avoiding sample damage and charging effects. Higher beam currents gave higher pattern intensity, but lower pattern quality. The working distance was set to 25.3 mm and the step size to 2 µm. The SEM was run in low vacuum mode to avoid both charging and the effects of carbon coating on the EBSD patterns. Data was collected offline at a rate of 50 frames per second. All the patterns were stored on a hard disk using the NORDIF 2.0 software and then indexed later on a computer using the TSL-OIM ver. 7.2 software. Because of the high resolution of the Hough, 0.25 degree step, 240 $\times$ 240 pixel resolution, and the many phases the indexing was considerably slower with a rate of 2–4 frames per second. Indexing was refined several times by adjusting the Hough settings in order to best index and distinguish the 9 phases. The confidence index for map production varied from phase to phase. Orthopyroxene generally had poorer patterns than the other minerals, resulting in less successful indexing, and incorrect indexing of clinopyroxene was common. Olivine had the best indexing with an estimated correct indexing of 99.5%. Subsequently, the data were processed using the open source Matlab toolbox MTEX 4.2.1 (Bachmann et al., 2010, 2011; Mainprice et al., 2015). To filter out incorrectly

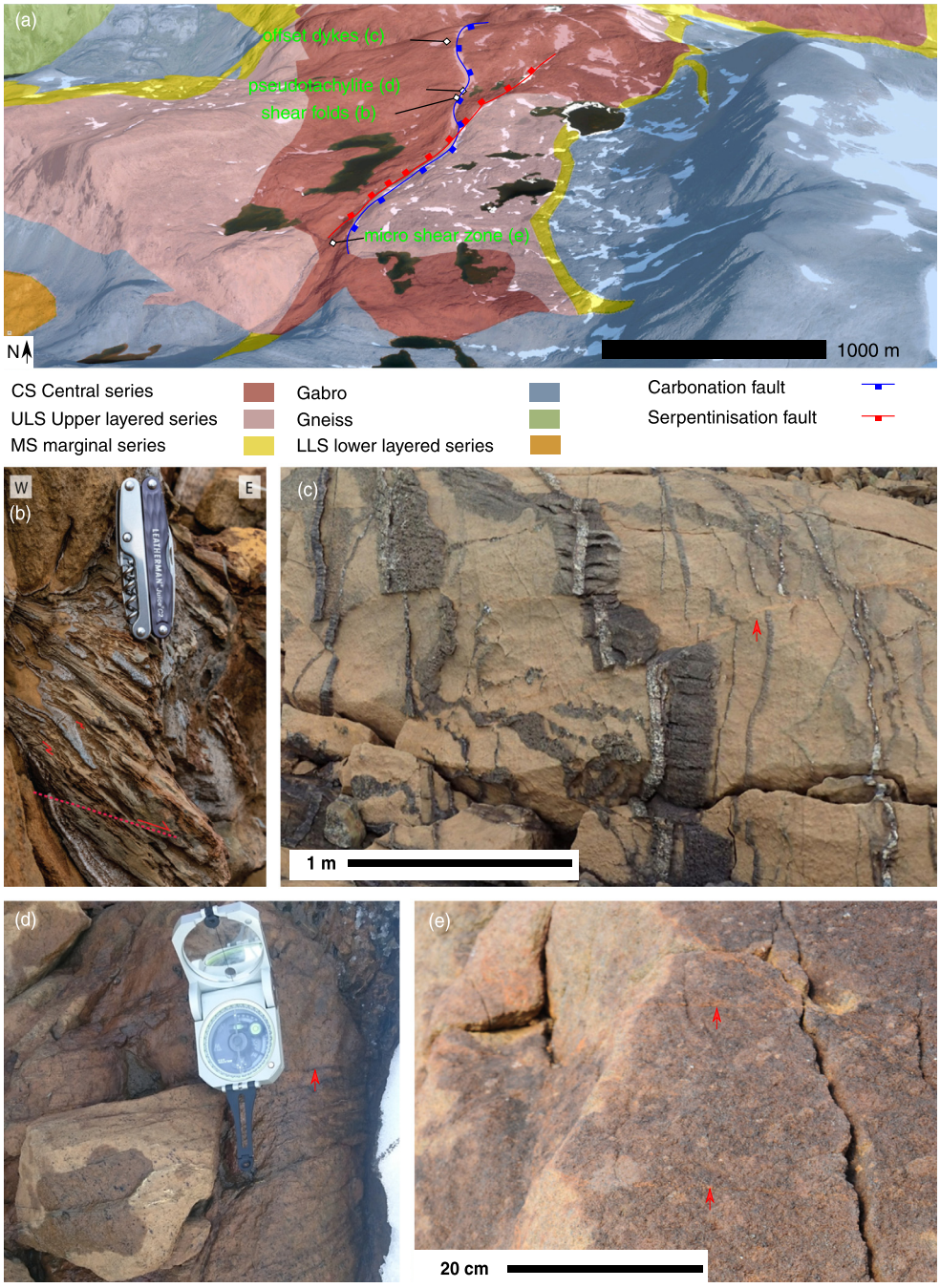

Fig. 1. Geological map and field observations. (a) of the Reinfjord intrusion. Major NS fault related to carbonation reactions drawn in blue. Later normal fault related to serpentinization drawn in red. Eastern block is inferred to have a downward movement on the carbonation fault, whereas the western block moved down on the serpentinization fault. Rock units are CS: central series, ULS: upper layered series, LLS: lower layered series. Modified after Larsen et al. (2018). The length of the carbonation fault is about 2 km. Letter label relates to field photographs b-e in this figure. (b) Asymmetric folds in the footwall of main fault show a down throw of the eastern block. (c) Micro shear zones offsetting dykes in complex pattern in footwall close to main fault. The micro shear zones are recognized both by their offset of the dykes and they have a more orange/yellow weathering color compared to the host rock. (d) Field image of the pseudotachylite sample, dark lines on the rock surface are serpentine veins and pseudotachylites. (e) Field image of micro shear zone sample. The micro shear zones are visible as orange colored lines on the weathered rock surface, which are barely recognizable in the field. (For interpretation of the colors in the figure(s), the reader is referred to the web version of this article.)

indexed points, a custom script was made in MTEX with specific success criteria based on pattern quality and confidence index for the different phases. Final processed maps were compared to SEM-backscatter and SEM-EDS maps to confirm the phase interpretation from the EBSD. The Grain-boundary discrimination angle was set to 5 degrees, as it showed the best agreement with pattern quality maps, with coherent low pattern quality lines representing grain-boundaries.

3.3. Phase diagram calculations

Phase diagrams were calculated using Perple_x version 6.8.0 (Connolly, 1990, 2005) using the 2011 version of the updated Holland and Powell (1998) thermodynamic database (Holland and Powell, 2011). Solution models for minerals orthopyroxene (Opx(HP)) and clinopyroxene (Cpx(HP)) (Holland and Powell, 1996), olivine (O(HP)) (Holland and Powell, 1998) and carbonate

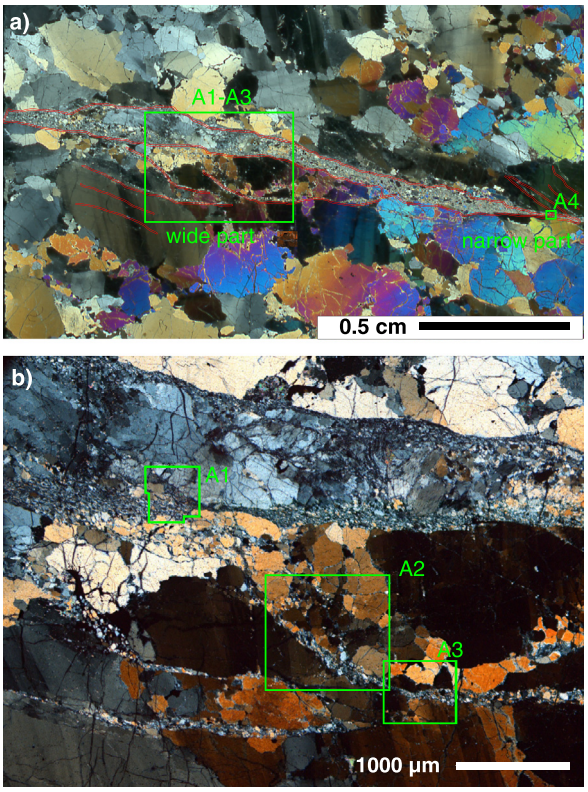

Fig. 2. Crossed polarized optical images of the micro shear zone sample thin section, locations of EBSD maps of wide part of micro shear zone (A1), Shear zone offshoot (A3) and narrow shear zone (A4) are marked with green boxes. a) View across the whole thin section displaying the variability in shear zone thicknesses from the wide part in the left. b) Area denoted by A1–A3 green box in a), with larger, 0.5 cm long. Areas mapped by EBSD, Backscatter and EDS are shown by numbered squares (A1, A2, A3, and A4) in figures a and b.

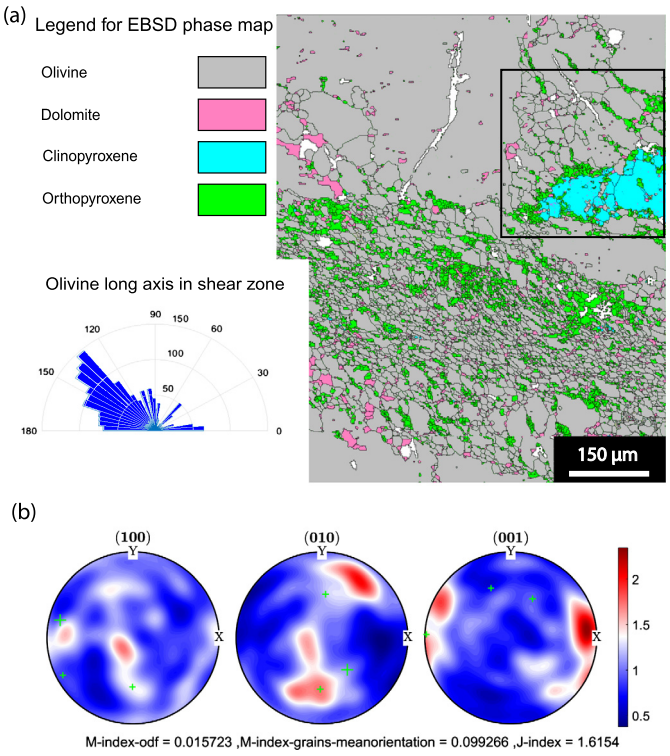

Fig. 3. EBSD phase map a) and pole figures of olivine in the central shear zone A1 in the wide part. Insert shows the SPO of grains in the shear zone. Black square denotes the location of the proximal part of the shear zone shown in Fig. 4. b) Pole figures of grains inside the central fine-grained part of the shear zone.

(Franzolin et al., 2011) were used in the calculation. A simplified version of the bulk composition was used to match both the product assemblage and the original bulk volume mineral proportions (Table S1). To calculate volume expansion due to mineral reaction during carbonation, two bulk compositions (with and without CO_2) were used. The outputs from Perple_x program *Werami* were processed in Matlab to obtain the volume change during carbonation reaction and compared to unreacted wehrlite at the given PT-conditions, assuming preservation of mass during reaction. The local volume changes were calculated by using the volumes of the products compared to the reactants actually involved in the reaction.

4. Results

4.1. Microstructural observations

Numerous samples taken from near the main faults contain micro shear zones. Here we focus on the best preserved micro shear zone sample, which contains features typical of the Reinfjord shear zones. The sample consists of large cumulus olivine (84 vol%) with interstitial clinopyroxene grains (16 vol%) and less than 1 vol% minor phases. In thin section, strain localization occurs in a 0.9 mm to 0.1 mm thick shear zone with very fine-grained material cutting though larger olivine grains (Fig. 2). Both the mineralogy and the SPO vary between the wide and narrow segments of the shear zone. An increase in internal deformation in the olivine adjacent to the shear zones is observed as deformation bands in microphotographs (Fig. 2). SEM and EBSD investigations show that in addition to being more fine-grained, the shear zone has a different modal mineralogy compared to the host rock, with dolomite and orthopyroxene filling the interstices between elongated olivine grains (Figs. 3–6). The amounts of secondary orthopyroxene and dolomite vary both across, and along the shear zone. In the central parts of the widest section of the shear zones, both orthopyroxene and dolomite are fine-grained with a mean grain size below 15 µm (Fig. S1). In the wide part of the shear zone, the dolomite grain size increases away from the shear zone center and dolomite and orthopyroxene grain-aggregates tend to form a network parallel to the SPO defined by the olivine grains (Figs. 3 and 4). Clinopyroxene grains are mantled by orthopyroxene in a flame-like structure, with the strings of orthopyroxene extending outward into large olivine grains, which are broken into several fragments, and separated by orthopyroxene and dolomite (Figs. 3 and 4). EBSD reveals that the new grains between the enstatite and dolomite can be divided into two groups based on Grain Orientation Spread (GOS) (Fig. 4b). In the first group, the grains show similar GOS as the parent grains, whereas the second group is characterized by lower GOS than the parent grains (Fig. 4b). Grains of the two groups have similar orientations, showing a clear orientation inheritance from the parent grains (Fig. 4c and d).

The shear zone offshoots, shown in Fig. 5 and Fig. S1, have similar characteristics to the host rock adjacent to the wide part of the shear zone, where fragments of broken old grains represented by grains with high grain orientation spread (GOS) and inherited orientations, and low GOS olivine grains with a new CPO. This is particularly visible in the (010) pole figure (Fig. 4c and d), where the parent-grain maxima on the edges of the pole figure, are shifted towards a more central maximum.

In contrast to the wide part of the shear zone, the narrow segments of the shear zone contain less orthopyroxene and dolomite and they preserve fine-grained clinopyroxene (Fig. 6). There is an

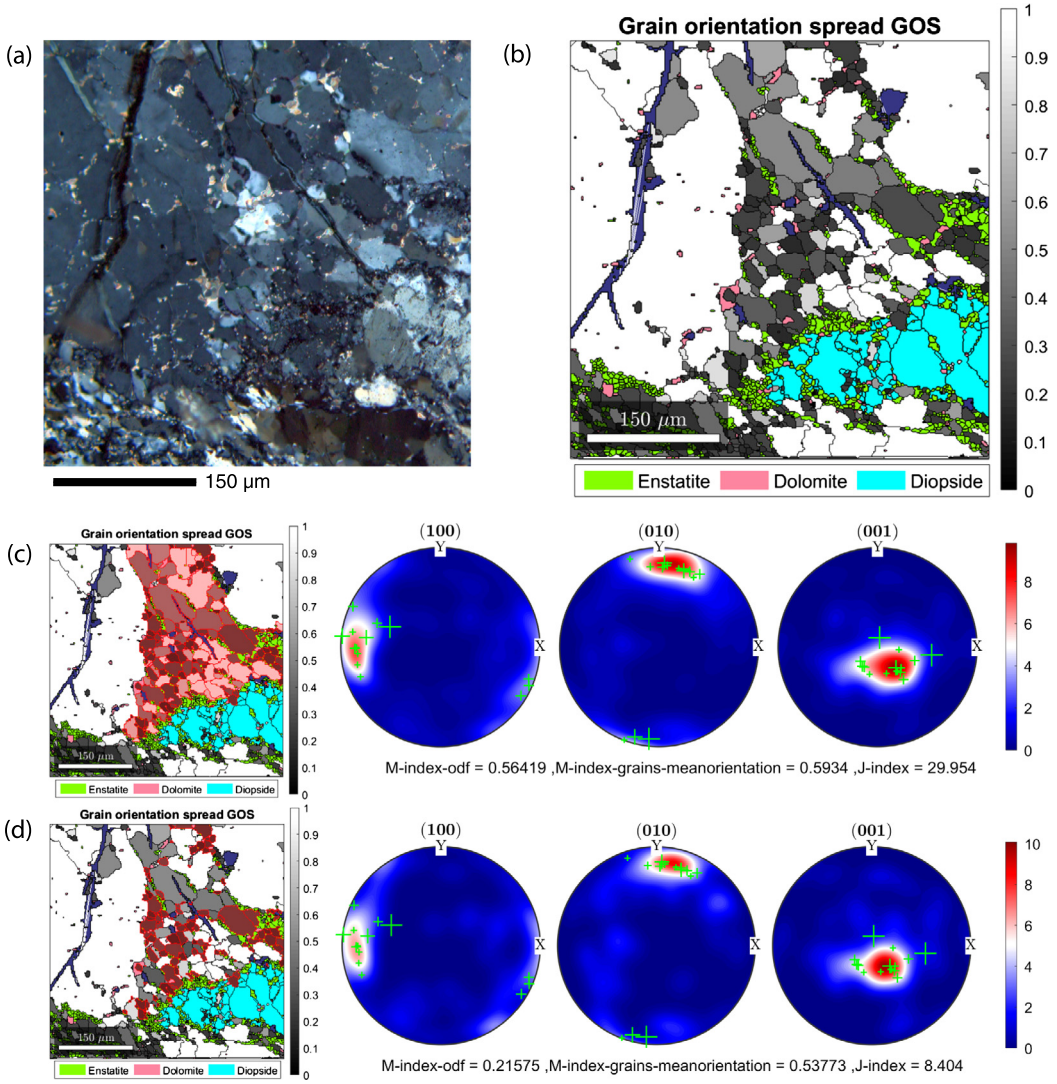

Fig. 4. Magnification of proximal part of the wide shear zone with optical and EBSD maps and olivine pole figures. a) Optical image. Few micro sized calcite grains are observed as bright inclusions in olivine and along sub-grain boundaries. b) Grayscale color-coded of olivine GOS and other phases colored according to legend. c) Pole figures of all grains in the more deformed area in the olivine grain. Grain selection marked with red. d) Pole figures of low GOS grains in more deformed in the large olivine grain. Grain selection marked with red in the insert to the left. Black crosses in the pole figures show orientations of the large surrounding grains.

abrupt transition from the fine-grained shear zone to the coarse-grained dunite outside the shear zone. This sharp change is in contrast to the wider part of the shear zone, where the transition is more gradual. The CPO in the narrow segment of the shear zone is weak, and shows an inheritance relationship with the remnants of larger parent grains. The SPO of olivine is also absent in the narrow part of the shear zone (Fig. 6).

4.2. Pressure-temperature calculations

Thermodynamic modeling reveals that the shear zones formed at high pressures and temperatures of at least 8 kb and 775 °C, respectively (Fig. 8a). The predicted reaction of olivine plus clinopyroxene to dolomite and enstatite is similar to those previously reported (Ueda et al., 2008; Wyllie et al., 1983). At this point it is not possible to precisely date the formation of the shear zones. However, the temperature estimates fall below those of the intrusion (Grant et al., 2016) and above those likely for Caledonian metamorphism (Gasser et al., 2015) (Fig. 8b). This suggests that the shear zones are pre-Caledonian, and most likely formed during cooling of the intrusion. From metamorphic grade and geometric relationships, it is clear that the shear zones are not related to later low-temperature (lizardite) serpentinization, which cuts the shear zones (Grant et al., 2017).

5. Discussion

5.1. Coupled deformation and fluid metasomatism

There is mounting evidence to suggest that deformation and mineral reactions are closely interlinked during strain localization (Incel et al., 2017; Newman et al., 1999). For example, quartz deformation has been documented as a result of dissolution-re-precipitation processes during H_2O infiltration into dry quartz-bearing rocks, giving rise to contrasting behavior in quartz grains over the distance of a few microns (Sørensen and Larsen, 2009). Similar behavior is documented in olivine, relating to OH defects in experimentally deformed olivine aggregates (Précigout and Stünitz, 2016). Mineral reactions, and the formation of secondary phases, and may lead to an increase in volume, and small increases can be sufficient to lead to significant fracturing (Røyne and Jamtveit, 2015).

The differences in modal mineralogy off the shear zones and the wall rock, namely the increases in dolomite and enstatite

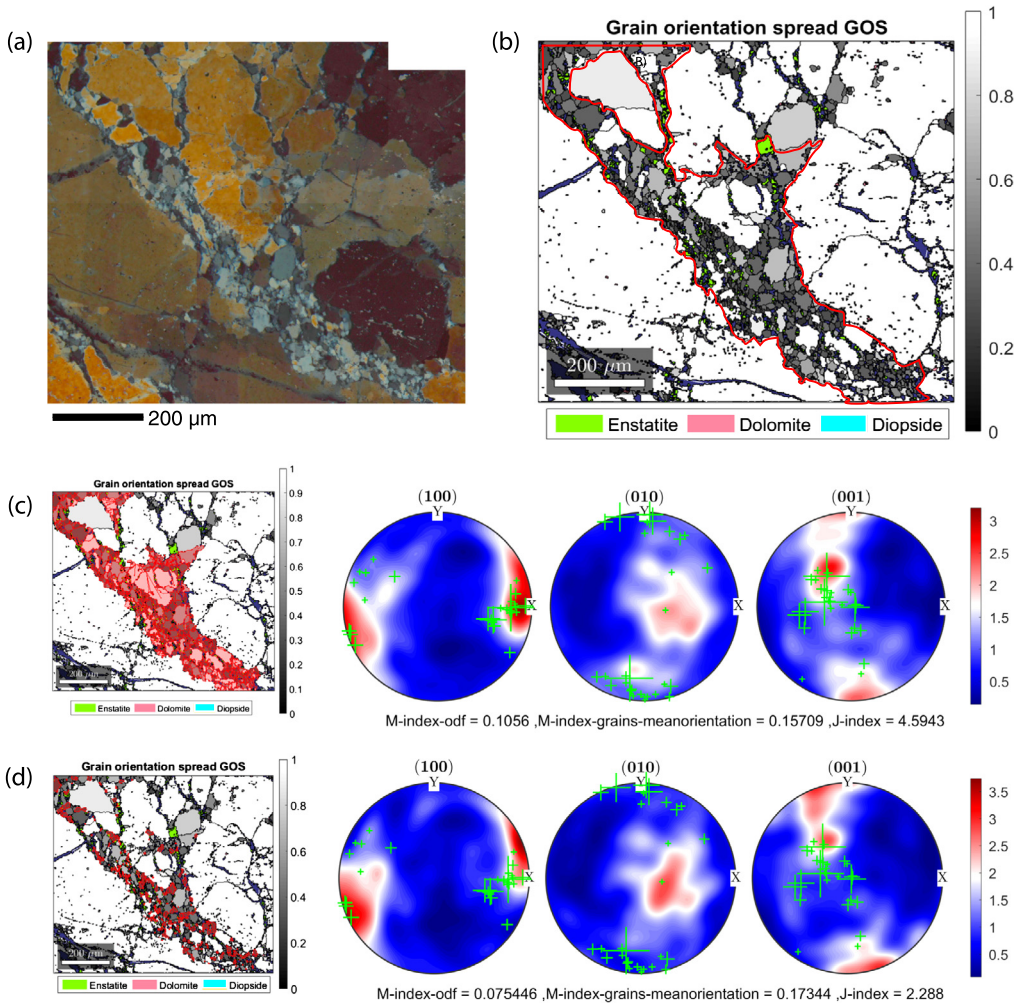

Fig. 5. EBSD maps and pole figures of olivine in the shear zone offshoot (A2-1) in the wide part of the shear zone. a) Optical image. Note that olivine grains and subgrains can be followed across the shear zone offshoot, indicating little or no displacement. b) Grayscale color-coded of olivine GOS and other phases colored according to legend. c) Pole figures of all grains in the shear zone offshoot. Grain selection marked with red. d) Pole figures of low GOS olivine grains in the shear zone offshoot. Grain selection marked with red in the insert to the left. Black crosses in the pole figures show orientations of the large surrounding grains.

at the expense of olivine and clinopyroxene, attest to the coupling between deformation and metasomatism via a CO_2-rich fluid. Late CO_2 bearing carbonate-rich alkaline melts metasomatize the ultramafic rocks of Reinfjord, producing slots of carbonate bearing assemblages and free CO_2-bearing fluids (Grant et al., 2016; Larsen et al., 2018). The assemblage of olivine + clinopyroxene + CO_2 is stable until, during cooling, a reaction boundary is passed with the formation of dolomite + enstatite and loss of olivine and clinopyroxene (Wyllie et al., 1983). When crossing the reaction curve (Fig. 8) an increase in bulk volume occurs, leading to fracturing. The addition of weaker secondary phases, in comparison to the primary phases, also leads to deformation and strain localization (Escartin et al., 2001; Herwegh et al., 2011; Linckens et al., 2011). The change in volume of the mineral assemblage during the formation of orthopyroxene and dolomite from olivine and clinopyroxene is 2.5 vol% in the bulk reacted volume with local volume increase of up to 7 vol%. Similar changes in volume and grain size reduction due to mineral reactions have been demonstrated to lead to the brittle failure in eclogite facies rocks (Incel et al., 2017). We suggest that a similar response occurs from the mineral volume expansion in our samples. These features may well be associated with pseudotachylites and paleo-earthquakes, as observed by Ueda et al. (2008) in the Ivrea zone, Italy.

The coupling between deformation and metasomatism provides an explanation for the complex variations in CPO, SPO and mineralogy observed across the shear zones. The changes in grain size and the localization of strain is discussed in more detail below.

5.2. Reduction in grain size and strain localization

5.2.1. Reaction-induced grain breakage

Mineral reaction led to grain size reduction as observed for dolomite and orthopyroxene products along olivine subgrain boundaries, with mean grain sizes dropping from mm-scale to tens of microns. Given that fluid mobility in the host rock must be limited by the high pressures and temperatures, volatiles are assumed to have been mobilized along shear zones. Because permeability will likely be reduced by recrystallization at high temperatures and pressures, volatile transport and reaction were probably concurrent with deformation.

Fusseis et al. (2009) documented how active shear zones generate a dynamic permeability during deformation in the diffusion creep regime by viscous grain-boundary sliding, creep cavitation, dissolution and precipitation. Such permeability has been documented by X-ray tomography (Fusseis et al., 2009; Menegon et al., 2015) and through C' type shear bands with weak CPO (Menegon

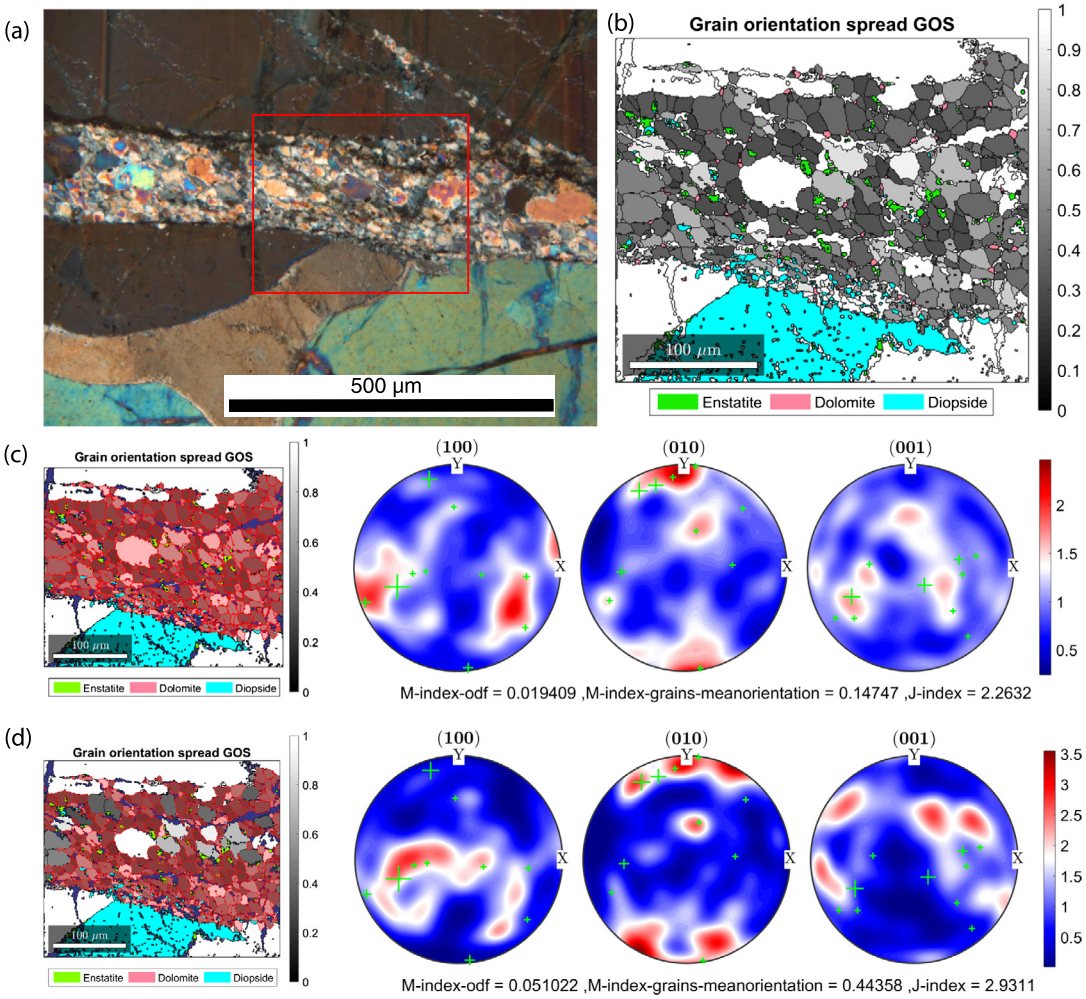

Fig. 6. EBSD maps and pole figures of the narrow part of the shear zone (A4). a) Optical image. Note the sharp boundary of the shear zone. Black box denotes the location of the EBSD map. b) Grayscale color-coded of olivine GOS and other phases colored according to legend. Note, portions of the upper grain are included in the shear zone, and the small clinopyroxene grains inside the shear zone have not reacted with the olivine. c) Pole figures of all olivine grains in the narrow shear zone. d) Pole figures of small olivine grains in the shear zone offshoot. Grain selection marked with red. Green crosses in the pole figures show orientations of the large surrounding grains.

et al., 2015). We suggest a similar model for the fluid transfer in the Reinfjord shear zones, necessary for continued reaction within the existing and propagating fracture and shear zone systems. Therefore, we infer that fluid flow occurred during active deformation, with syntectonic carbonate mineral reaction forming orthopyroxene and dolomite. The volume expansion of reaction in the deforming shear zone is thus likely to induce fracturing and strain localization in fracture systems promoted by local fluid overpressure.

5.2.2. *Relation between grain size and rheology*

The grain size reduction induced by mineral reactions during early stages of deformation may be responsible for a change in deformation processes and rock rheology. Experimental data document strain localization in fine-grained domains in olivine aggregates under constant stress boundary conditions (Hansen et al., 2012). Localized deformation then leads to focused mechanical work inducing even finer grain sizes, leading to larger strength contrast between the coarse and fine-grained domains (Hansen et al., 2012). Though strains are often assumed to be uniform in large-scale tectonic models, according to large scale convergence rates, these convergence rates may be accomplished by heterogeneous strain rates with varying shear zone thicknesses at constant stress (Platt and Behr, 2011). As specific domains become more fine-grained, strain localization and local strain rate increase as shear zones become thinner. Additionally, as grain size decreases, the deformation mechanism evolves from dislocation creep to grain-size sensitive creep, in the form of dislocation-accommodated grain boundary sliding (disGBS) and diffusion-accommodated grain boundary sliding (difGBS) (Fig. 9a).

In our samples, the lack of CPO and the lack of correlation between CPO strength and grain-size reduction are best explained by difGBS deformation. DifGBS, in contrast, leads to CPO development, which may lead to seismic anisotropy (Hansen et al., 2016, 2011; Ohuchi et al., 2015). In many respects, our observations in the shear zones match those associated with diffusion creep and GBS reported in the literature, such as CPO weakening in the fine-grained domains and existence of large olivine fragments in the fine-grained matrix (Drury et al., 2011; Fliervoet et al., 1999; Menegon et al., 2015; Précigout and Stünitz, 2016; Torgersen et al., 2015; Warren and Hirth, 2006).

The change in grain size from the host rock with mm-cm sized olivine grains to the micro shear zones with approximately 10 μm olivine grains, results in a change in deformation mechanism from dislocation creep, as indicated by subgrains in the wall rock, to disGBS, or difGBS in the fine-grained shear zones. This change in deformation is consistent with deformation mechanism maps calculated using a modified version of the MATLAB scripts of Warren and Hirth (2006), implementing the flow laws for dry olivine (Hirth and Kohlstedt, 2003). The grain-size reduction and

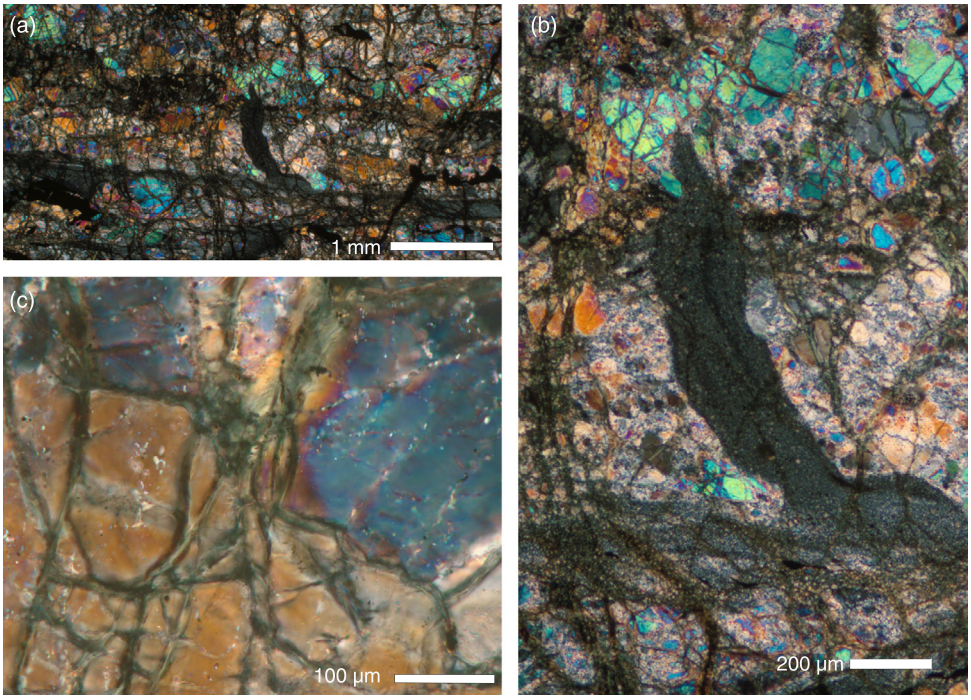

Fig. 7. Optical textures of the pseudotachylite bearing samples. a) Overview of micro shear zone with veins of pseudotachylite material. b) Close-up of the pseudotachylite vein intruding into a large, pervasively fractured olivine grain with grain size <1.5 µm. c) Carbonate-rich CO_2 inclusions comprised by CO_2 and carbonates in large olivine grains.

the resulting decrease in strength, leads to a more than two orders of magnitude increase in strain rate, possibly as much as 10^{-9}/s (Fig. 9). Toy et al. (2010) reported similar observations in ultramafic rocks from the Twin Sisters Massif in Washington, where strain localization in dunite along clinopyroxenite and orthopyroxenite dikes is caused by grain size reduction due to mineral reactions near the dikes.

5.2.3. Role of the secondary phases in rheology

Another important factor controlling deformation is the strength of the newly crystallizing phases in the shear zone. Experimental data indicate that the strength of dolomite is an order of magnitude lower than olivine (Holyoke et al., 2014). However, as dolomite does not form an interconnected network in the flow plane of the shear zones. Thus, we assume that the properties of olivine dominated the rheology.

The grain-boundary pinning of olivine due to the presence of secondary phases (opx and dol) is also important for the overall rheology. The widely distributed orthopyroxene and dolomite in the grain aggregate may have limited olivine grain growth, and hence maintained the fine grain size in the high strain domain, promoting strain softening. Herwegh et al. (2011) reviewed the effects of secondary phases in the grain size and rheology of polymineral samples. In their studies, minor amounts of secondary phases resulted in behavior similar to those of the matrix phase, whereas larger amounts of secondary phases changed the properties of the deforming aggregate through the pinning of grain boundary movement of the primary phase. This would also result in a finer dynamically recrystallized grain size than predicted by grain size paleo piezometers that are based on dynamic recrystallization processes. The grain-size of olivine is approximately 10 µm equivalent circle diameter (EQD) for both the narrow and wide parts of the shear zone centers. The grain-size of the secondary phases averaging about 5 µm. The Zener parameter (Z) was calculated according to the method of (Herwegh et al., 2011), according to the equation $Z = dp/fp$, where dp is the grain size and fp is the volume fraction of secondary phases. The calculated Zener parameter of in the wide and narrow part of the shear zone was 28 and 22 respectively. Plotted in Zener diagrams, the Reinfjord data are well within the field controlled by secondary phases, at even finer grain sizes than reported in the literature (Herwegh et al., 2011; Linckens et al., 2011) (Fig. 9).

Not only do the secondary phases preserve the fine grain size, thereby maintaining the weak and preferentially deformed shear zone, mineral reactions along sub-grain boundaries also lead to grain sizes at least two orders of magnitude lower than in the original rock. The sub-grain structures in the larger olivine grains are the result of dislocation creep in the coarser grained parts of the rock. Strain localization in the fine-grained domains may lead to the incorporation of almost all the strain within these domains. Strain localization may lead to ultrafast deformation and the formation of the pseudotachylites, which also show evidence of carbonate-rich CO_2 bearing fluids as micro-inclusions intersecting larger olivine grains (Fig. 7).

5.3. Relation between shear zones, fluid flow, magmatic CO_2 and earthquakes in the lower crust and upper mantle

It has been demonstrated that lower crust and upper mantle fluids are CO_2-rich (Frezzotti and Touret, 2014; Larsen et al., 1998; Touret and Huizenga, 2012). This may be related to pervasive fluxing of CO_2 from the mantle (Frezzotti and Touret, 2014) in magmatic environments, or the intrusion of CO_2 bearing magmas at the base of the crust (Lee et al., 2016; Pili et al., 1999; Takeuchi and Arai, 2015). More specifically, CO_2-bearing fluids were observed in association with contact metamorphism, and later granulite facies metamorphism in the nearby Øksfjord Peninsula (Elvevold and Andersen, 1993). This highlight the regional importance of CO_2 in the SIP. The origin of the CO_2-bearing fluids in granulite facies rocks in the Øksfjord Peninsula is poorly constrained; however, a significant amount of CO_2 may have been transported from the mantle to the lower crust by the alkaline, mafic and ultramafic melts that form the SIP (Larsen et al., 2018). Carbonatite complexes in the SIP have isotopic signatures (Nd,

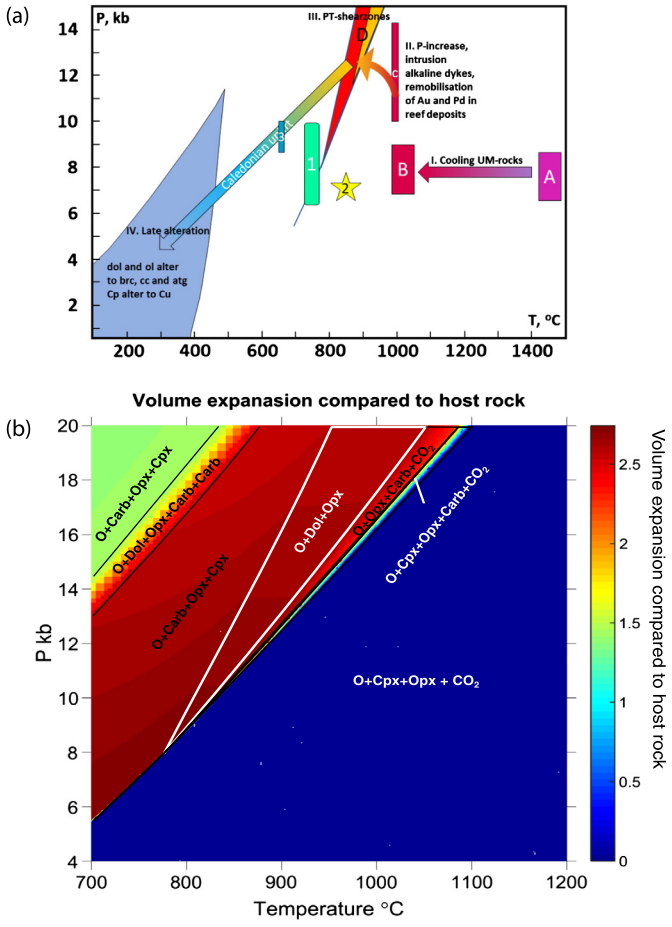

Fig. 8. P-T-path of the Reinfjord complex. (a) The apparent P-T loop of the Reinfjordultramafic complex with Caledonian data from the Hasvik gabbro consisting of (1) The pre-intrusion temperature, (2) Conditions of contact metamorphism, (A) P-T of the picritic/komatiitic melts, (B) Cooling temperatures of the Reinfjord complex from two-pyroxene thermometry, (C) crystallization temperatures of lamproitic dykes, (D) P-T from pseudosections of extensional shear zones, (III) PT condition of the Caledonian uplift from the Hasvik gabbro and (IV) Late alteration of dolomite and olivine to form brucite + calcite and chalcopyrite to form native copper. Modified after Larsen et al., 2018. (b) Detailed pseudosection of the shear zone assemblages, based on stability of orthopyroxene + olivine + dolomite assemblage and volume expansion compared to volatile free rock. Calculated with Perplex version 677 and HP11 database using Opx(W), Ol(HP), Cpx(HP) and carbonate (odCcMS(EF)) solution models. Abbreviation in diagram olivine (O), clinopyroxene (Cpx), Orthopyroxene (Opx), Carbonate solid solution (Carb).

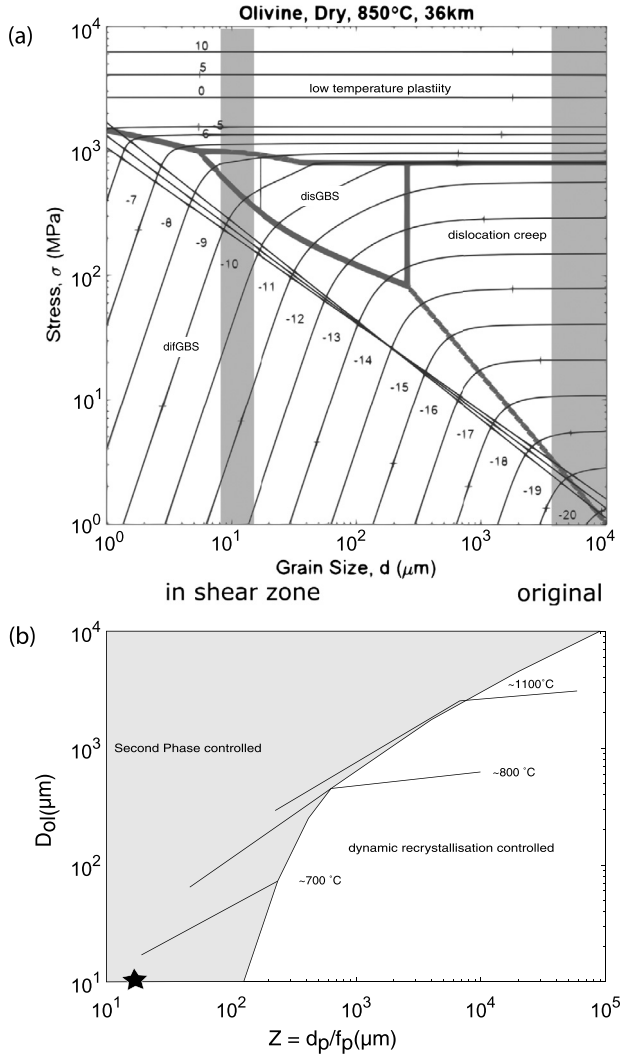

Fig. 9. (a) Deformation mechanism maps after Warren and Hirth (2006). Shaded grey areas mark the grain size (fine grained) and in the original rock and in the shear zone (coarse grains). (b) The shear zone sample Zener diagram after (Herwegh et al., 2011), lines denote the results from different temperatures (Herwegh et al., 2011), and micro shear zone sample is marked by the black star. See text for discussion.

Hf, O, C, S) that strongly suggest they originated in the mantle (Larsen et al., 2018; Roberts et al., 2010; Wulff-Pedersen, 1992). Furthermore, the presence of clots and veins of carbonate-bearing magmatic assemblages observed throughout the ultramafic rocks in Reinfjord, indicates infiltration by late stage alkaline melts in the intrusion enriched in CO_2 (Larsen et al., 2018).

Mantle-derived CO_2 lost from the mantle may be transported through lithospheric scale fault systems extending down into the mantle (Pili et al., 1999), as evident from the co-seismic mantle derived CO_2 emissions from fault zones in the East-African Rift (Hunt et al., 2017; Lee et al., 2016; Weinstein et al., 2017). The role of CO_2 in shear zone formation has been demonstrated in rocks from the upper crust to lower crustal granulites (Pili et al., 1997, 1999), in upper mantle rocks (Ueda et al., 2008) and here proposed in lower crustal to upper mantle ultramafic rift-related intrusions in association with the infiltration of volatile-rich alkaline melts. This study shows that CO_2 within shear zones initiates localized shear zone development in ultramafic rocks via a coupled deformation-metasomatic process. Propagation of CO_2 along shear zones initiates further deformation at shallower levels of the crust, providing a pathway for further fluid migration and resulting in a positive feedback mechanism. Hence faults acts as conduits where mantle-derived CO_2 emissions are then pumped through the active fault system.

We propose that a coupled deformation – metasomatic reaction between CO_2 and peridotite is the most likely mechanism that resulted in faulting and possibly seismicity in Reinfjord during the post-magmatic cooling phase in the late history of the intrusion.

6. Conclusions

- CO_2 was a common volatile in the Reinfjord system, introduced together with juvenile asthenospheric mantle melts.
- CO_2 reaction with ultramafic rocks induced mineral reactions, which involved large changes in volume. Local expansion lead to fracturing of larger grains along sub grain boundaries and a reduction in grain size.
  - This reduces rock strength and increases strain rates by two orders of magnitude.
  - Local increased strain rates induces very high deformation rates which in turn facilitates formation of pseudotachylites.

- Despite few other reports of carbonated mantle shear zones, we expect that the processes observed in Reinfjord are common in lower crustal and mantle shear zones typically associated with continental extension and rifting. The signature mineral assemblages decompose during exhumation, particularly the carbonated assemblages. Commonly, the only surviving evidence are CO_2 fluid inclusions in olivine originating from decarbonation reactions during exhumation.
- The observed link between seismicity (pseudotachylites) and the carbonated mineral assemblages provides a model for deep crustal and upper mantle earthquakes in active rift zones, such as the East African Rift, where lower crustal and upper mantle rocks are infiltrated by CO_2-rich magmas. This is supported by the observations of co-seismic mantle-CO_2 emissions along deep normal faults in magmatic rifts of E Africa and N Zealand.

Acknowledgments and Data

Jamie Connolly suggested the Franzolin et al. thermodynamic model for the carbonates. Dr. Grants Post-doctoral studies are funded in the ABYSS Program by the People Program (Marie Curie Actions) of the European Union's Seventh Framework Programme FP7/2007-2013/ under REA Grant Agreement n° 608001. We are indebted to the Department of Geosciences and Petroleum (NTNU) for contributing with supplementary funding when needed. Oddmund Hansen in Reinfjord was an indispensable help on site in the Reinfjord Village. Comments and suggestions by Andreas K. Kronenberg and an anonymous reviewer improved the readability and scientific impact of this manuscript.

Appendix A. Supplementary material

Supplementary material related to this article can be found online at https://doi.org/10.1016/j.epsl.2019.115713.

References

Bachmann, F., Hielscher, R., Schaeben, H., 2010. Texture analysis with MTEX–free and open source software toolbox. Solid State Phenom. 160, 63–68.

Bachmann, F., Hielscher, R., Schaeben, H., 2011. Grain detection from 2d and 3d EBSD data-specification of the MTEX algorithm. Ultramicroscopy 111 (12), 1720–1733. https://doi.org/10.1016/j.ultramic.2011.08.002.

Balmforth, N.J., Craster, R.V., Rust, A.C., 2005. Instability in flow through elastic conduits and volcanic tremor. J. Fluid Mech. 527, 353–377. https://doi.org/10.1017/S0022112004002800.

Brune, S., Williams, S.E., Müller, R.D., 2017. Potential links between continental rifting, CO_2 degassing and climate change through time. Nat. Geosci. 10 (12), 941–946. https://doi.org/10.1038/s41561-017-0003-6.

Canil, D., 1990. Experimental study bearing on the absence of carbonate in mantle-derived xenoliths. Geology 18 (10), 1011–1013.

Canil, D., Scarfe, C.M., 1990. Phase-relations in peridotite + CO_2 systems to 12 GPa – implications for the origin of kimberlite and carbonate stability in the Earths upper mantle. J. Geophys. Res. B, Solid Earth Planets 95 (B10), 15805–15816.

Chen, Y., Hjelen, J., Gireesh, S.S., Roven, H.J., 2012. Optimization of EBSD parameters for ultra-fast characterization. J. Microsc. 245 (2), 111–118. Retrieved from <Go to ISI>://WOS:000298987100001 http://onlinelibrary.wiley.com/store/10.1111/j.1365-2818.2011.03551.x/asset/j.1365-2818.2011.03551.x.pdf?v=1&t=inhg50wg&s=ece7a07081be0fa96e97735213a4b29c4743b9f5.

Connolly, J.A.D., 1990. Multivariable phase diagrams: an algorithm based on generalized thermodynamics. Am. J. Sci. 290. https://doi.org/10.2475/ajs.290.6.666.

Connolly, J.A.D., 2005. Computation of phase equilibria by linear programming: a tool for geodynamic modelling and its application to subduction zone decarbonation. Earth Planet. Sci. Lett. 236. https://doi.org/10.1016/j.epsl.2005.04.033.

Dixon, J.E., 1997. Degassing of alkalic basalts. Am. Mineral. 82, 368–378.

Drury, M.R., Avé Lallemant, H.G., Pennock, G.M., Palasse, L.N., 2011. Crystal preferred orientation in peridotite ultramylonites deformed by grain size sensitive creep, Étang de Lers, Pyrenees, France. J. Struct. Geol. 33 (12), 1776–1789. https://doi.org/10.1016/j.jsg.2011.10.002.

Elvevold, S., Andersen, T., 1993. Fluid evolution during metamorphism at increasing pressure: carbonic- and nitrogen-bearing fluid inclusions in granulites from Øksfjord, north Norwegian Caledonides. Contrib. Mineral. Petrol. 114 (2), 236–246. https://doi.org/10.1007/BF00307758.

Escartin, J., Hirth, G., Evans, B., 2001. Strength of slightly serpentinized peridotites: implications for the tectonics of oceanic lithosphere. Geology 29 (11), 1023–1026.

Fliervoet, T.F., Drury, M.R., Chopra, P.N., 1999. Crystallographic preferred orientations and misorientations in some olivine rocks deformed by diffusion or dislocation creep. Tectonophysics 303 (1), 1–27. https://doi.org/10.1016/S0040-1951(98)00250-9.

Foley, S.F., Fischer, T.P., 2017. An essential role for continental rifts and lithosphere in the deep carbon cycle. Nat. Geosci. 10 (12), 897–902. https://doi.org/10.1038/s41561-017-0002-7.

Franzolin, E., Schmidt, M., Poli, S., 2011. Ternary Ca–Fe–Mg carbonates: subsolidus phase relations at 3.5 GPa and a thermodynamic solid solution model including order/disorder. Contrib. Mineral. Petrol. 161 (2), 213–227.

Frezzotti, M.-L., Touret, J.L.R., 2014. CO_2, carbonate-rich melts, and brines in the mantle. Geosci. Front. 5 (5), 697–710. https://doi.org/10.1016/j.gsf.2014.03.014.

Fusseis, F., Regenauer-Lieb, K., Liu, J., Hough, R., De Carlo, F., 2009. Creep cavitation can establish a dynamic granular fluid pump in ductile shear zones. Nature 459 (7249), 974.

Gasser, D., Jeřábek, P., Faber, C., Stünitz, H., Menegon, L., Corfu, F., Whitehouse, M.J., et al., 2015. Behaviour of geochronometers and timing of metamorphic reactions during deformation at lower crustal conditions: phase equilibrium modelling and U–Pb dating of zircon, monazite, rutile and titanite from the Kalak Nappe Complex, northern Norway. J. Metamorph. Geol. 33 (5), 513–534.

Gerlach, T., McGee, K., Elias, T., Sutton, A., Doukas, M., 2002. Carbon dioxide emission rate of Kīlauea Volcano: implications for primary magma and the summit reservoir. J. Geophys. Res., Solid Earth 107 (B9).

Grant, T.B., Larsen, R.B., Anker-Rasch, L., Grannes, K.R., Iljina, M., McEnroe, S., Øen, E., et al., 2016. Anatomy of a deep crustal volcanic conduit system; the Reinfjord Ultramafic Complex, Seiland Igneous Province, Northern Norway. Lithos 252–253 (Suppl. C), 200–215. https://doi.org/10.1016/j.lithos.2016.02.020.

Grant, T.B., McEnroe, S., Sørensen, B.E., Larsen, R., Pastore, Z., Grannes, K.R., Nikolaisen, E., 2017. Serpentinization and carbonation of pristine continental ultramafic rocks and applications. to the oceanic crust; H_2O–CO_2 alteration of dunites and re-distribution of Ni-Cu-PGE. in sulphide deposits.

Hansen, L.N., Warren, J.M., Zimmerman, M.E., Kohlstedt, D.L., 2016. Viscous anisotropy of textured olivine aggregates, part 1: measurement of the magnitude and evolution of anisotropy. Earth Planet. Sci. Lett., 445(Suppl. C), 92–103. https://doi.org/10.1016/j.epsl.2016.04.008.

Hansen, L.N., Zimmerman, M.E., Dillman, A.M., Kohlstedt, D.L., 2012. Strain localization in olivine aggregates at high temperature: a laboratory comparison of constant-strain-rate and constant-stress boundary conditions. Earth Planet. Sci. Lett. 333, 134–145.

Hansen, L.N., Zimmerman, M.E., Kohlstedt, D.L., 2011. Grain boundary sliding in San Carlos olivine: flow law parameters and crystallographic-preferred orientation. J. Geophys. Res., Solid Earth 116 (B8). https://doi.org/10.1029/2011JB008220.

Herwegh, M., Linckens, J., Ebert, A., Berger, A., Brodhag, S., 2011. The role of second phases for controlling microstructural evolution in polymineralic rocks: a review. J. Struct. Geol. 33 (12), 1728–1750.

Hirth, G., Kohlstedt, D., 2003. Rheology of the upper mantle and the mantle wedge: a view from the experimentalists. In: Inside the Subduction Factory. American Geophysical, Union, pp. 83–105.

Holland, T., Powell, R., 1996. Thermodynamics of order-disorder in minerals, II: symmetric formalism applied to solid solutions. Am. Mineral. 81, 1425.

Holland, T., Powell, R., 2011. An improved and extended internally consistent thermodynamic dataset for phases of petrological interest, involving a new equation of state for solids. J. Metamorph. Geol. 29 (3), 333–383.

Holland, T.J.B., Powell, R., 1998. An internally consistent thermodynamic data set for phases of petrological interest. J. Metamorph. Geol. 16. https://doi.org/10.1111/j.1525-1314.1998.00140.x.

Holyoke, C.W., Kronenberg, A.K., Newman, J., Ulrich, C., 2014. Rheology of magnesite. J. Geophys. Res., Solid Earth 119 (8), 6534–6557.

Hunt, J.A., Zafu, A., Mather, T.A., Pyle, D.M., Barry, P.H., 2017. Spatially variable CO_2 degassing in the Main Ethiopian Rift: implications for magma storage, volatile transport, and rift-related emissions. Geochem. Geophys. Geosyst. 18 (10), 3714–3737. https://doi.org/10.1002/2017gc006975.

Incel, S., Hilairet, N., Labrousse, L., John, T., Deldicque, D., Ferrand, T., Schubnel, A., et al., 2017. Laboratory earthquakes triggered during eclogitization of lawsonite-bearing blueschist. Earth Planet. Sci. Lett. 459 (Suppl. C), 320–331. https://doi.org/10.1016/j.epsl.2016.11.047.

Larsen, R.B., Eide, E.A., Burke, E.A.J., 1998. Evolution of metamorphic volatiles during exhumation of microdiamond-bearing granulites in the Western Gneiss Region, Norway. Contrib. Mineral. Petrol. 133 (1), 106–121. https://doi.org/10.1007/s004100050441.

Larsen, R.B., Grant, T., Sørensen, B.E., Tegner, C., McEnroe, S., Pastore, Z., Michels, A., et al., 2018. Portrait of a giant deep-seated magmatic conduit system: the Seiland Igneous Province. Lithos 296–299 (Suppl. C), 600–622. https://doi.org/10.1016/j.lithos.2017.11.013.

Lee, H., Muirhead, J.D., Fischer, T.P., Ebinger, C.J., Kattenhorn, S.A., Sharp, Z.D., Kianji, G., 2016. Massive and prolonged deep carbon emissions associated with continental rifting. Nat. Geosci. 9 (2), 145–149. https://doi.org/10.1038/ngeo2622.

Linckens, J., Herwegh, M., Müntener, O., Mercolli, I., 2011. Evolution of a polymineralic mantle shear zone and the role of second phases in the localization of deformation. J. Geophys. Res., Solid Earth (1978–2012) 116 (B6).

Lindenfeld, M., Rümpker, G., Batte, A., Schumann, A., 2012. Seismicity from February 2006 to September 2007 at the Rwenzori Mountains, East African Rift: earthquake distribution, magnitudes and source mechanisms. Solid Earth 3 (2), 251–264. https://doi.org/10.5194/se-3-251-2012.

Mainprice, D., Bachmann, F., Hielscher, R., Schaeben, H., 2015. Descriptive tools for the analysis of texture projects with large datasets using MTEX: strength, symmetry and components. Geol. Soc. (Lond.) Spec. Publ. 409, SP409.408.

Menegon, L., Fusseis, F., Stünitz, H., Xiao, X., 2015. Creep cavitation bands control porosity and fluid flow in lower crustal shear zones. Geology 43 (3), 227–230.

Moen, K., Hjelen, J., Malvik, T., 2003. Preparation of Quartz samples for EBSD analysis. Helsinki. Paper presented at the Applied Mineralogy.

Newman, J., Lamb, W.M., Drury, M.R., Vissers, R.L., 1999. Deformation processes in a peridotite shear zone: reaction-softening by an H_2O-deficient, continuous net transfer reaction. Tectonophysics 303 (1), 193–222.

Ohuchi, T., Kawazoe, T., Higo, Y., Funakoshi, K.-I., Suzuki, A., Kikegawa, T., Irifune, T., 2015. Dislocation-accommodated grain boundary sliding as the major deformation mechanism of olivine in the Earth's upper mantle. Sci. Adv. 1 (9). https://doi.org/10.1126/sciadv.1500360. e1500360-e1500360.

Okubo, P.G., Wolfe, C.J., 2008. Swarms of similar long-period earthquakes in the mantle beneath Mauna Loa Volcano. J. Volcanol. Geotherm. Res. 178 (4), 787–794.

Pili, E., Sheppard, S.M., Lardeaux, J.-M., Martelat, J.-E., Nicollet, C., 1997. Fluid flow vs. scale of shear zones in the lower continental crust and the granulite paradox. Geology 25 (1), 15–18.

Pili, E., Sheppard, S.M.F., Lardeaux, J.-M., 1999. Fluid-rock interaction in the granulites of Madagascar and lithospheric-scale transfer of fluids. Gondwana Res. 2 (3), 341–350. https://doi.org/10.1016/S1342-937X(05)70271-9.

Platt, J.P., Behr, W.M., 2011. Grainsize evolution in ductile shear zones: implications for strain localization and the strength of the lithosphere. J. Struct. Geol. 33 (4), 537–550. https://doi.org/10.1016/j.jsg.2011.01.018.

Précigout, J., Stünitz, H., 2016. Evidence of phase nucleation during olivine diffusion creep: a new perspective for mantle strain localisation. Earth Planet. Sci. Lett.

Prior, D.J., Mariani, E., Wheeler, J., 2009. EBSD in the earth sciences: applications, common practice, and challenges. In: Electron Backscatter Diffraction in Materials Science. Springer, pp. 345–360.

Reyners, M., Eberhart-Phillips, D., Stuart, G., 2007. The role of fluids in lower-crustal earthquakes near continental rifts. Nature 446 (7139), 1075–1078.

Roberts, R.J., Corfu, F., Torsvik, T.H., Ashwal, L.D., Ramsay, D.M., 2006. Short-lived mafic magmatism at 560–570 Ma in the northern Norwegian Caledonides: U–Pb zircon ages from the Seiland Igneous Province. Geol. Mag. 143 (6), 887–903. https://doi.org/10.1017/S0016756806002512.

Roberts, R.J., Corfu, F., Torsvik, T.H., Hetherington, C.J., Ashwal, L.D., 2010. Age of alkaline rocks in the Seiland Igneous Province, Northern Norway. J. Geol. Soc. 167 (1), 71–81. https://doi.org/10.1144/0016-76492009-014.

Roecker, S., Ebinger, C., Tiberi, C., Mulibo, G., Ferdinand-Wambura, R., Mtelela, K., Peyrat, S., et al., 2017. Subsurface images of the Eastern Rift, Africa, from the joint inversion of body waves, surface waves and gravity: investigating the role of fluids in early-stage continental rifting. Geophys. J. Int. 210 (2), 931–950. https://doi.org/10.1093/gji/ggx220.

Rovetta, M.R., Blacic, J.D., Delaney, J.R., 1987. Microfracture and crack healing in experimentally deformed peridotite. J. Geophys. Res., Atmos. 92 (B12), 12902–12910. https://doi.org/10.1029/JB092iB12p12902.

Rovetta, M.R., Delaney, J.R., Blacic, J.D., 1986. A record of high-temperature embrittlement of peridotite in CO_2 permeated xenoliths from basalt. J. Geophys. Res., Solid Earth (1978–2012) 91 (B3), 3841–3848.

Røyne, A., Jamtveit, B., 2015. Pore-scale controls on reaction-driven fracturing. Rev. Mineral. Geochem. 80 (1), 25–44.

Sørensen, B.E., Larsen, R.B., 2009. Coupled trace element mobilisation and strain softening in quartz during retrograde fluid infiltration in dry granulite protoliths. Contrib. Mineral. Petrol. 157 (2), 147–161.

Takeuchi, M., Arai, S., 2015. Upper mantle can in-situ fracture: an implication from a cataclastic peridotite xenolith from Megata, Northeast Japan arc. Mineral. Petrol. 109 (2), 283–294.

Torgersen, E., Viola, G., Sandstad, J., Stein, H., Zwingmann, H., Hannah, J., 2015. Effects of frictional–viscous oscillations and fluid flow events on the structural evolution and Re–Os pyrite–chalcopyrite systematics of Cu-rich carbonate veins in northern Norway. Tectonophysics 659, 70–90.

Touret, J.L.R., Huizenga, J.M., 2012. Fluid-assisted granulite metamorphism: a continental journey. Gondwana Res. 21 (1), 224–235. https://doi.org/10.1016/j.gr.2011.07.022.

Toy, V.G., Newman, J., Lamb, W., Tikoff, B., 2010. The role of pyroxenites in formation of shear instabilities in the mantle: evidence from an ultramafic ultramylonite, twin sisters massif, Washington. J. Petrol. 51 (1–2), 55–80. https://doi.org/10.1093/petrology/egp059.

Ueda, T., Obata, M., Di Toro, G., Kanagawa, K., Ozawa, K., 2008. Mantle earthquakes frozen in mylonitized ultramafic pseudotachylytes of spinel-lherzolite facies. Geology 36 (8), 607–610.

Warren, J.M., Hirth, G., 2006. Grain size sensitive deformation mechanisms in naturally deformed peridotites. Earth Planet. Sci. Lett. 248 (1), 438–450. https://doi.org/10.1016/j.epsl.2006.06.006.

Weinstein, A., Oliva, S.J., Ebinger, C.J., Roecker, S., Tiberi, C., Aman, M., Fischer, T.P., et al., 2017. Fault-magma interactions during early continental rifting: seismicity of the Magadi-Natron-Manyara basins, Africa. Geochem. Geophys. Geosyst. 18 (10), 3662–3686. https://doi.org/10.1002/2017gc007027.

Wignall, P.B., 2001. Large igneous provinces and mass extinctions. Earth-Sci. Rev. 53 (1), 1–33.

Wilshire, H., Kirby, S., 1989. Dikes, joints, and faults in the upper mantle. Tectonophysics 161 (1), 23–31.

Wulff-Pedersen, E., 1992. Petrological and Metamorphic Evolution of Carbonate Lithologies on Øksfjordhalvøya, N. Norway. Master Thesis (in Norwegian). University of Tromsø.

Wyllie, P., Huang, W.-L., Otto, J., Byrnes, A., 1983. Carbonation of peridotites and decarbonation of siliceous dolomites represented in the system $CaO–MgO–SiO_2–CO_2$ to 30 kbar. Tectonophysics 100 (1), 359–388.